

UCLA

UCLA Previously Published Works

Title

Facet-Dependence of Electron Storage in Gold-Decorated Titania Nanocrystals

Permalink

<https://escholarship.org/uc/item/6q29475k>

Journal

Chemistry of Materials, 35(22)

ISSN

0897-4756

Authors

Son, Giyeong

Li, Yichen

Shneidman, Anna V

et al.

Publication Date

2023-11-28

DOI

10.1021/acs.chemmater.3c01252

Copyright Information

This work is made available under the terms of a Creative Commons Attribution-NonCommercial-NoDerivatives License, available at

<https://creativecommons.org/licenses/by-nc-nd/4.0/>

Peer reviewed

Facet-Dependence of Electron Storage in Gold-Decorated Titania Nanocrystals

Giyeong Son,¹ Yichen Li,² Anna V. Shneidman,¹ Jae Hyo Han,¹ Michael Aizenberg,¹ Philippe Sautet,^{2,3*} and Joanna Aizenberg^{1,4*}

¹John A. Paulson School of Engineering and Applied Sciences, Harvard University, Allston, Massachusetts 02134, United States

²Department of Chemistry and Biochemistry, University of California, Los Angeles, California 90095, United States

³Department of Chemical and Biomolecular Engineering, University of California, Los Angeles, California 90095, United States

⁴Department of Chemistry and Chemical Biology, Harvard University, Cambridge, Massachusetts 02138, United States

KEYWORDS: *facet-dependent electron charge storage, photocharging storage, interfacial charge transfer, dark catalysis*

ABSTRACT: A variety of materials have been developed over the last two decades with the goal of extending the function of light-absorbing devices to low-light or nighttime conditions. Typically, this requires storage of photogenerated charges, which depends on a variety of physicochemical features including the crystallographic nature of materials interfaces, which we investigate here. We implemented a model system consisting of gold nanoparticles (AuNPs) supported on titanium dioxide (TiO₂) anatase nanocrystals with predominantly {101}, {100} or {001} facets. Cyclic voltammetry in dark, anaerobic conditions showed that all three materials exhibited increased current densities with increasing illumination time, with highest increase in Au/TiO₂{001}. We further employed photocharged Au/TiO₂ particles for catalytic reactions in the dark, and found a consistent trend of Au/TiO₂{001} being the most active. Using density functional theory, we calculated the Bader charge and the partial density of states, revealing that the presence of additional oxygen atoms at the Au/TiO₂ interface leads to charge depletion from the Au, providing more accessible vacant states to accept electrons from TiO₂. Our results suggest that the crystal surface engineering can be used as a powerful tool to optimize materials for electron charge storage.

Introduction

With an ever-growing global concern regarding climate change and the use of fossil fuels, it is crucial to develop new technologies that can effectively harness renewable energies. This entails first capturing and then storing the energy; in solar applications, specifically, this requires absorption of energy from the sun or other illumination source followed by storing photogenerated charge carriers to be used in functions such as production of electricity (i.e. in photovoltaics and solar cells) or to perform oxidation and reduction reactions (i.e. in photocatalysts). While absorbing materials have undergone decades of research and development,^{1,2} materials that can store energy from light absorbed during illumination and delay the function to night or low-light conditions more generally are in their infancy.

The ability to conduct photocatalytic reactions well after illumination has been terminated was first demonstrated in the early 2000s using tungsten oxide (WO₃) supported on titania (TiO₂). The authors demonstrated that the electrons generated within TiO₂ upon light irradiation spilled over to WO₃, thereby preventing electron-hole recombination or other similarly non-productive exciton decay pathways.³⁻⁵ This opened investigations in what is now often referred to as “energy storage”,

“dark”, “memory”, or “persistent” photocatalysis.^{6,7} Since then, numerous materials combinations have been investigated,⁸⁻¹² including metal nanoparticles (NPs) supported on metal oxide (MOx) supports, which are of general interest in the fields of catalysis, plasmonics, and sensing, to name a few.¹³⁻¹⁵

While photocatalysis post irradiation has been demonstrated for several metal NP/MOx support combinations,⁸⁻¹⁰ there has not yet been much attention dedicated to the facet-dependence of their charge-storage effect, despite the now well-known fact that faceting of nanocrystals affects their photophysical and catalytic properties.¹⁶ For example, it has been shown that the {001} family of facets of anatase TiO₂ nanocrystals can facilitate oxidation reactions since the extra surface OH groups on this facet provide hole-trapping sites through the generation of surface-bound OH radicals.¹⁷ Meanwhile, {101} facets coexisting with {001} generally act as a reduction site due to the difference in the conduction band levels of the two interfaces.¹⁸ Moreover, metal NPs (e.g. Au, Pt) on the {001} facets of TiO₂ can facilitate photocatalytic water oxidation to a greater extent than when they are deposited on {101} due to the influence of metal NPs coordination on the specific interfacial structures of oxide supports in different crystallographic directions.¹⁹

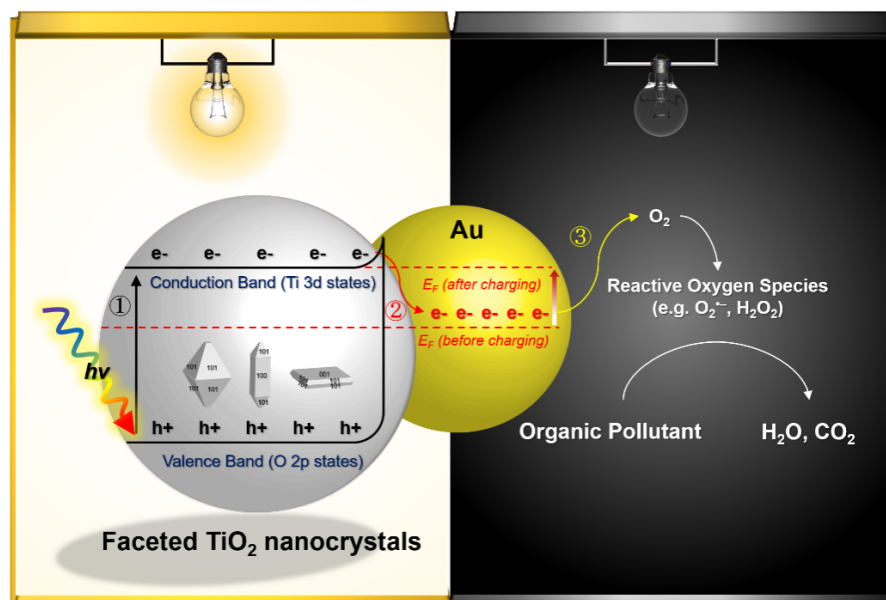


Figure 1. Illustration of light-induced electron charging enabled by gold nanoparticles (AuNPs) immobilized on titanium dioxide (TiO₂) nanocrystals with different exposed facets. (1) Following light irradiation (left), photo-excited electrons from TiO₂ transfer to AuNPs states, causing (2) an increase in the Fermi level of the AuNPs. (3) These electrons can then be transferred to oxygen to generate reactive oxygen species (O₂^{•-}, H₂O₂), even in the dark (right), resulting in the decomposition of organic pollutants, if present.

Here, we investigate how faceting affects the ability of a metal/metal oxide system to store photogenerated charges and perform redox reactions in the dark. Gold nanoparticles (AuNPs) supported on TiO₂ anatase nanocrystals were used as a model system (**Figure 1**) as titania is widely known as an excellent photoactive material and gold nanoparticles are commonly employed as co-catalysts on TiO₂ to help separate electrons from holes and limit their fast recombination.^{20,21} To study how the photogenerated electron storage ability of this materials system depends on specific faceting, we synthesized three types of TiO₂ nanocrystals with predominantly exposed (101), (100), or (001) surfaces, henceforth called TiO₂(101), TiO₂(100), and TiO₂(001), respectively.²² Following the attachment of AuNPs on the surface of the nanocrystals, we determined that Au/TiO₂(001) generated the highest photogenerated current of the three. The production of reactive oxygen species and degradation of methylene blue were then studied as model photocatalytic reactions post irradiation for different durations and at different light intensities. Again, the Au/TiO₂(001) particles were found to be the most reactive in the dark. We explain these differences through density functional theory (DFT) analysis of the Au/TiO₂ interface. We determined that Au/TiO₂(001) has the most interfacial oxygen adatoms compared to the other two materials systems. A calculation of the electronic density of states confirmed that the more oxygen-rich interface leads to a larger proportion of vacant states in the Au available for electron capture and storage from the TiO₂.

Results

Synthesis and characterization of different faceted TiO₂ and Au/TiO₂.

The synthesis of the Au/TiO₂ particles is described in detail in the *Methods* section. It involves two steps, wherein the three types of anatase TiO₂ nanocrystals were first synthesized, and

then a ligand-exchange method was used to attach AuNPs (**Figure 2a**). Transmission electron microscopy (TEM) imaging revealed that the TiO₂ nanocrystals were (1) bipyramidal, 400 +/- 100 nm in length (a total of n=20 particles were measured for statistics), (2) rod-shaped, 500 +/- 200 nm in length (n=20), and (3) nanoplates of 100 +/- 30 nm width (n=20) (**Figure 2b, c, d** and **Figure S1, S2, S3, S4**).^{23,24} The facet distributions were calculated following a previously-reported method as ~99% exposed {101} family of facets for the bipyramidal particles (henceforth referred to as TiO₂(101)), ~85% {100} for the rods (TiO₂(100)), and ~86% {001} for the nanoplates (TiO₂(001)); see **SI Note S1** and **Figure S4** for details on the procedure for calculating the relative surface area occupied by the different facets. TEM analysis showed that the synthesized AuNPs had a diameter of 9.5 nm +/- 0.5 (n=10), and that all of the particles retained their shapes and sizes after deposition of 1.5 wt% of the AuNPs on the surface of each type of TiO₂ nanocrystal (**Figure 2e, f, g, h, i, j**). The AuNPs appeared light red in solution and had an LSPR absorption band around 516 nm (**Figure S5**). By measuring the optical density of the supernatant at this wavelength following the ligand-exchange process, we found that almost all the AuNPs were successfully attached to the TiO₂ nanocrystals regardless of TiO₂ shape (**Figure S6**).

Light-induced electron storage

We used electrochemical analyses to assess the charge storage ability of the three types of Au/TiO₂. The different TiO₂ nanocrystals without (control) and with AuNPs were deposited on indium tin oxide (ITO) electrodes and illuminated by an Xe lamp for 0, 2, 5 or 10 min in anaerobic conditions to suppress water oxidation and the resulting generation of reactive oxidative species (see *Materials and Methods* for details). Upon terminating the irradiation, we conducted cyclic voltammetry (CV) in the dark also under anaerobic conditions. The bare TiO₂ nanocrystals showed negligible changes in their CV curves in

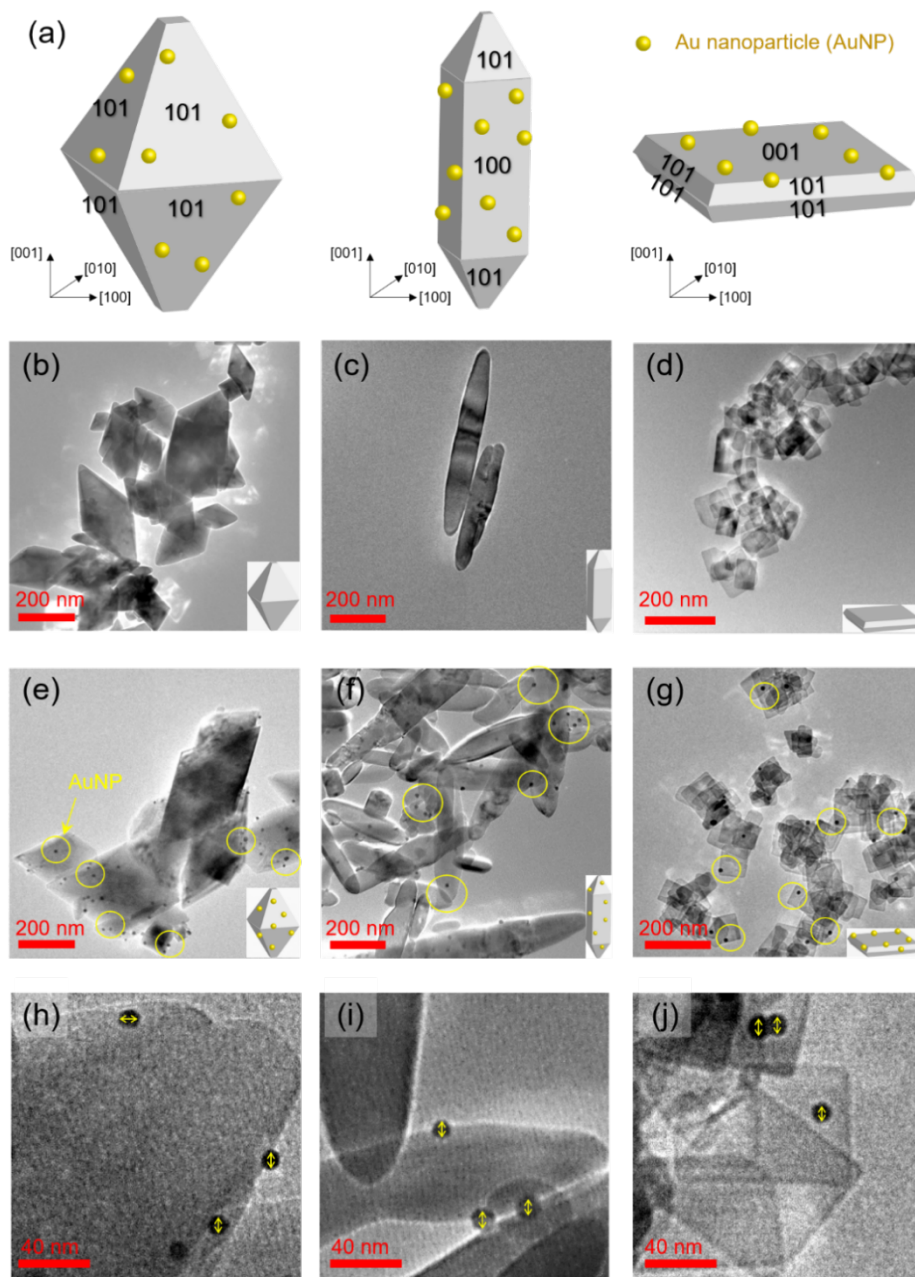


Figure 2. Assessing the morphology of gold-decorated titania nanocrystals. (a) Schematics of the faceting of the three different anatase TiO_2 nanocrystals (NCs) with AuNPs supported on them. (b-j) TEM images of the different TiO_2 NCs (bipyramidal, nanorod, and nanoplate, from left to right), without (b-d) and with (e-j) AuNPs. Gold NPs are highlighted by the yellow circles in (e-g) and their size is highlighted by the yellow double arrow in (h-j). The average diameter of AuNPs was measured to be $9.5 \text{ nm} \pm 0.5$ (number of particles assessed $n=10$).

the dark after light irradiation and this did not change upon increasing the irradiation time (**Figure 3a, b, c**). In contrast, the current densities for all of the Au/ TiO_2 materials increased following light irradiation (**Figure 3d, e, f**). The current densities under illumination for those particles started to increase at around 0.65 V (*vs.* Ag/AgCl), corresponding to the oxidation onset potential of AuNPs (**Figure S7**). The peak current densities at the oxidation potential (0.8 V *vs.* Ag/AgCl) gradually rose with increasing illumination time: from 4.0 without illumination up to $9.7 \mu\text{A}/\text{cm}^2$ after 10 min irradiation for Au/ $\text{TiO}_2(101)$, 4.2 to $12.8 \mu\text{A}/\text{cm}^2$ for Au/ $\text{TiO}_2(100)$, and, greatest of all, 5.1 to $20.2 \mu\text{A}/\text{cm}^2$ for Au/ $\text{TiO}_2(001)$.

We also calculated the specific capacitances for each of the tested materials from their respective voltage profiles (**Figure 4a, Note S2, Figure S8**). The value only very slightly increased for the bare TiO_2 nanocrystals following photocharging, while those for the Au/ TiO_2 increased substantially: the specific capacitance of Au/ $\text{TiO}_2(001)$ showed the greatest increase from 15.0 to 67.5 mF/g , compared to Au/ $\text{TiO}_2(100)$ and Au/ $\text{TiO}_2(101)$, whose specific capacitances rose from 8.3 to 37.3 and 7.8 to 22.4 mF/g , respectively. These results indicate that nanoplate TiO_2 decorated with AuNPs (i.e. Au/ $\text{TiO}_2(001)$) has the highest light-induced electron storage ability compared to the cases with nanorod and bipyramidal TiO_2 .

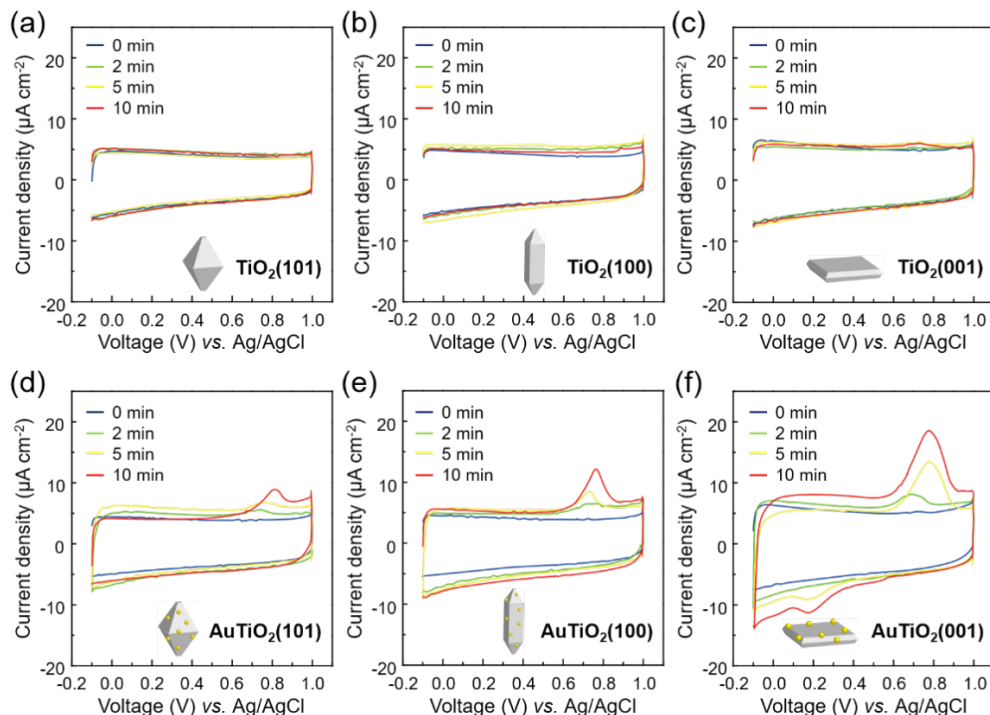


Figure 3. Electrochemical analysis of photoinduced electron storage behavior of differently faceted TiO₂ nanocrystals without (a-c) and with (d-f) AuNPs. The data represents the cyclic voltammetry (CV) measurements performed under anaerobic and dark conditions after following light irradiation for a duration if 0, 2, 5, or 10 min, as indicated by the legend.

We further investigated the charging and discharging processes of photocharged Au/TiO₂ by monitoring the photocurrent decay in dark, aerobic conditions following light irradiation in anaerobic conditions. As expected, the photoactivity of Au/TiO₂ during light irradiation was substantially higher than for all control TiO₂ samples (**Figure 4b**, inset) or for gold alone (**Figure S9**), typically attributed to the Schottky junction between AuNPs and Ti-O, which augments the resonant plasmonic absorption of AuNPs on the surface of TiO₂.^{25,26} The photocurrent density of Au/TiO₂(001) reached 23 μA/cm² at 0.7 V (vs. Ag/AgCl), 3 times higher than that of bare TiO₂(001) (7.5 μA). The current decayed for Au/TiO₂(001), with a time constant of 40 s (vs. 2 s for the bare TiO₂, **Figure 4b**). Similar charging and discharging profiles were observed for Au/TiO₂(101), and Au/TiO₂(100) (**Figure S10**). We found that following photocharging and discharging, the Au/TiO₂ returned to their initial discharged state (**Figure 4c, d and Figure S11**). In fact, we could cycle the materials with almost no signs of deterioration. For example, on the fifth charge/discharge cycle, we measured a decrease of the peak current density of less than 2 μA/cm² compared to the value measured in the first cycle (**Figure 4e, f**).

DFT studies on facet-dependent interface between Au and TiO₂

We employed density functional theory (DFT) to examine the nature of interface between the AuNPs and anatase TiO₂ substrates to determine the origins in the differences in the ability of Au/TiO₂(101), Au/TiO₂(100) and Au/TiO₂(001) to store photogenerated electrons. To be computationally tractable, the AuNP was modeled as a periodic one-dimensional Au rod representing the {111} family of facets. The rod is infinite along the TiO₂ [010] direction, 3 Au atomic rows in width and 3 rows in height (**Figure 5a and Figure S12**). The substrate was modeled

as p(2×2) 4-layer anatase TiO₂(001) surface with lattice constants $a = 3.82 \text{ \AA}$, $c = 9.52 \text{ \AA}$, and the fcc Au rod with $a = 4.15 \text{ \AA}$ lattice constant was adhered to the substrate along the [010] direction to minimize lattice mismatch (**Figure S12**). The Au rod and the top TiO₂ layer were relaxed. Similar models were also constructed on p(2×4) 3-layer TiO₂(101) and p(4×2) 4-layer TiO₂(100) surfaces (**Figure S13**). It has been previously shown that the presence of interfacial oxygen adatoms leads to stabilization of the interface and downshift of the Fermi level.²⁷ This results in a depletion of electrons from the AuNP, thereby creating vacant electronic states within the NP.²⁸ Given this, we sought to determine the optimal interfacial oxygen adatom coverage for each of the three types of Au/TiO₂ interfaces. The most stable interface for a given set of external conditions (e.g. temperature, pressure) is the one with lowest Gibbs free energy of formation:

$$\Delta G = E_{\text{AuO}_x/\text{TiO}_2} - E_{\text{Au}/\text{TiO}_2} - \frac{1}{2}\mu_{\text{O}_2}$$

where $E_{\text{Au}/\text{TiO}_2}$ and $E_{\text{AuO}_x/\text{TiO}_2}$ are the DFT-calculated energies in the pristine state or with oxygen adatoms, respectively; and μ_{O_2} is the chemical potential of O₂, which is a function of temperature and O₂ partial pressure (see **Note S3**). Vibrational entropy was assumed to be negligible. We implemented the calculations for Au/TiO₂(101), (100), and (001) with different numbers of interfacial oxygen adatoms (**Figure 5b**). Several sites for the adatoms were considered, including at the buried Au/TiO₂ interface (i.e. between the gold rod and the TiO₂ surface), at the Au/TiO₂ interface edge, and on the exposed TiO₂ surface, as well as on the Au (111), (100) and (110) surfaces. We found that the most stable interface for Au/TiO₂(101) under experimental conditions ($T = 298 \text{ K}$, $p_{\text{O}_2} = 21 \text{ kPa}$) is the one with 4 oxygen adatoms at the interface edge

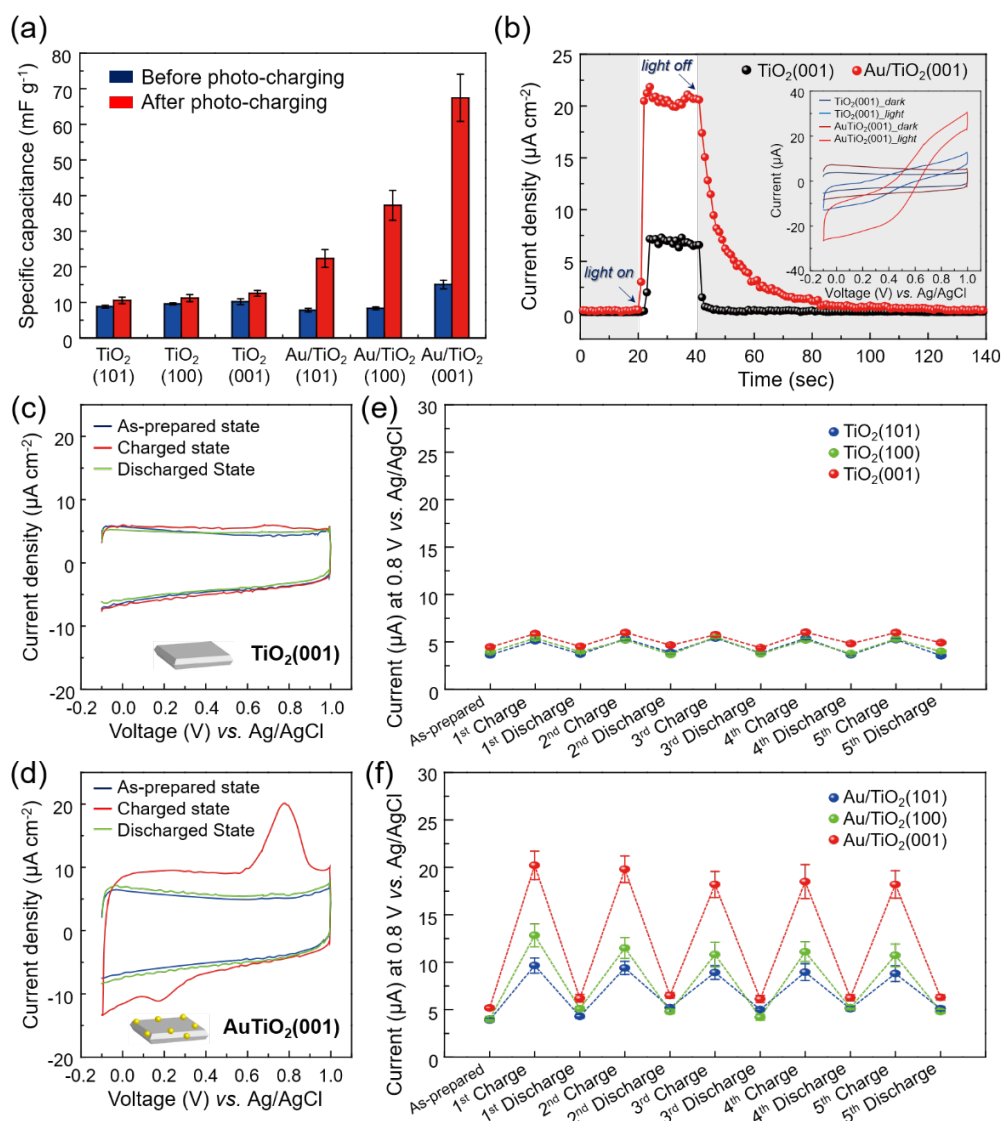


Figure 4. Assessment of specific capacitance, discharge process, and cyclability of the different Au/TiO₂ combinations. (a) Specific capacitance of all types of charged and uncharged TiO₂ and Au/TiO₂ nanocrystals. (b) Photocurrent before, during, and after light irradiation of TiO₂(001) and Au/TiO₂(001) at 0.7 V vs. Ag/AgCl. Inset: CV curves of TiO₂(001) and Au/TiO₂(001) under dark and light conditions. Chronoamperometry (CA) measurements were performed under anaerobic conditions. (c-d) Cyclic voltammetry (CV) curves of (c) TiO₂(001) and (d) Au/TiO₂(001) in their as-prepared, charged and discharged states. (e-f) Current of all three types of Au/TiO₂ at 0.8 V vs. Ag/AgCl according to the as-prepared, charged and discharged states. The charge-discharge current of the (e) TiO₂ and (f) Au/TiO₂ particles for the first through the fifth cycles. All currents were measured under anaerobic condition. Discharging was performed by flowing air. Charging time: 10 min irradiation. Discharging time: 10 min in the dark.

along the [010] direction (**Figure 5c**, vertical dashed line indicates experimental conditions). For Au on the more reactive TiO₂(100) surface,²⁹ the most stable interface at experimental conditions was found to be the one with 8 oxygen adatoms at the interface edges along [010] (**Figure 5d**). On the most reactive TiO₂(001) surface,²⁹ the most stable Au/TiO₂ interface consists of 12 oxygen adatoms distributed across the entire Au/TiO₂ interface (**Figure 5e**). These results show that the oxidation state of Au/TiO₂ interfaces under the experimental conditions is surface-structure sensitive and in the descending order of Au/TiO₂(001), Au/TiO₂(100), and Au/TiO₂(101). This trend coincides with TiO₂ surface energies, since the surface energies of (001), (100) and (101) are also in the descending order of 0.98, 0.58 and 0.49 J/m²;²⁹ the most unstable TiO₂(001) surface is

thereby most stabilized by the interfacial oxygen adatoms. Similar interfacial oxidation of Au rod on rutile TiO₂(110) has also been recognized in previous theoretical studies.^{28, 30, 31}

Given these results, we calculated the partial density of states (PDOS) for the Au rods on the different TiO₂ substrates with different numbers of interfacial oxygens (**Figure S14**) in order to understand the impact of the oxidation of the interface on the electronic structure of the system; the comparison of the PDOS for the most reactive TiO₂(001) surface with 0 or 12 interface oxygens is shown in **Figure 5f**. The Fermi level of the pristine Au rod on TiO₂(001) is just below the TiO₂ conduction band. According to the calculated net Bader charge distribution (representing how electrons are partitioned on different atoms),

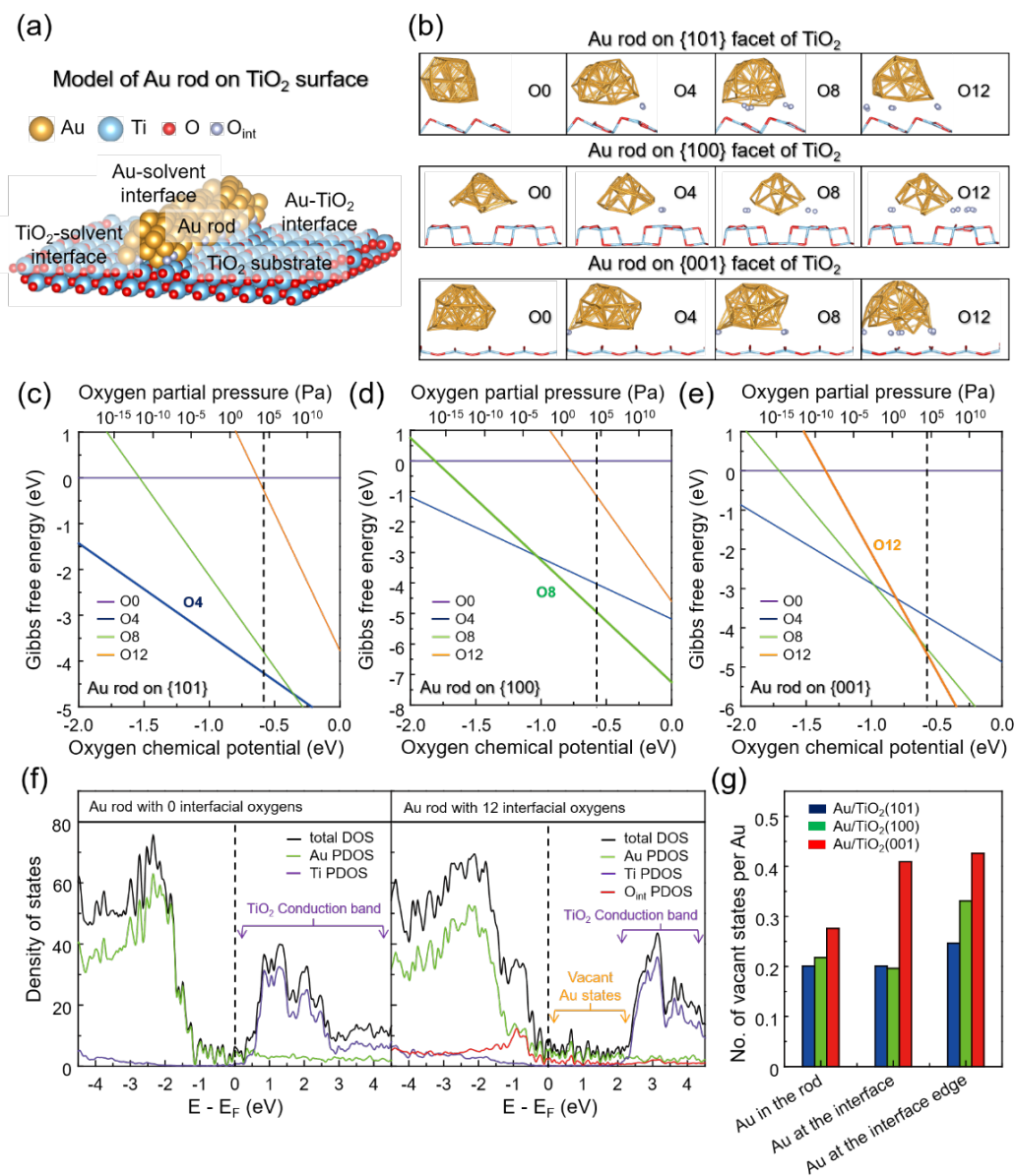


Figure 5. DFT calculations for Au nanorods on TiO₂(101), (100) and (001) surfaces. (a) Illustration of the Au rod on a TiO₂(001) surface. (b) Side views of the Au rod on TiO₂ facets along [010], with different numbers of interfacial oxygens. (c-e) Gibbs free energies as a function of oxygen partial pressure for Au rods on the different TiO₂ facets for different values of interfacial oxygens. Dashed lines indicate experimental conditions ($T = 298\text{K}$, $p_{\text{O}_2} = 21\text{ kPa}$). (f) Partial density of states for the Au rod on the TiO₂(001) facet with 0 (left) or 12 (right) interfacial oxygens. (g) Number of vacant states for Au atoms at different locations in the rod.

in the absence of interfacial oxygens, the electron transfer between the Au rod and TiO₂ substrate is small, and both weakly partially positive and negative Au atoms occur at the interface ($\sim\pm 0.1\text{ e}$) depending on the extent of lattice alignment with the substrate (Figure S15a). The oxygen adatoms provide additional states deep in the TiO₂ valence band, resulting in electron transfer from initially occupied Au gap states to those oxygen states (Figure 5f). A marked increase of the cationic nature of interfacial Au is also observed as a charge of up to $\sim +0.8\text{ e}$ for those Au atoms is determined from the net Bader charge distribution (Figure S15b). Au rods on TiO₂(101) and (100) facets show similar electron transfer from the Au nanorod to interfacial oxygens. These results show that the oxidation of the

Au/TiO₂ interface by oxygen adatoms creates vacant Au states for electron storage.

We calculated the number of vacant states for each Au atom on the three different TiO₂ facets to assess their ability to accept electrons (Figure 5g) and found that the number of vacant states per Au within the rod and at the interface is similar for both TiO₂(100) and (101) substrates. Meanwhile, the number of vacant states per Au at the interface edge (but not the rod bulk) on TiO₂(001) is $\sim 30\%$ larger than for the others. For the (001) substrate, Au atoms have 0.276, 0.409 and 0.426 vacant states in the rod, at the interface, and at the interface edge, respectively. The calculated electron storage ability of AuNPs on the family of TiO₂ facets hence follows the order $\{001\} > \{100\} > \{101\}$, supporting the experimental results.

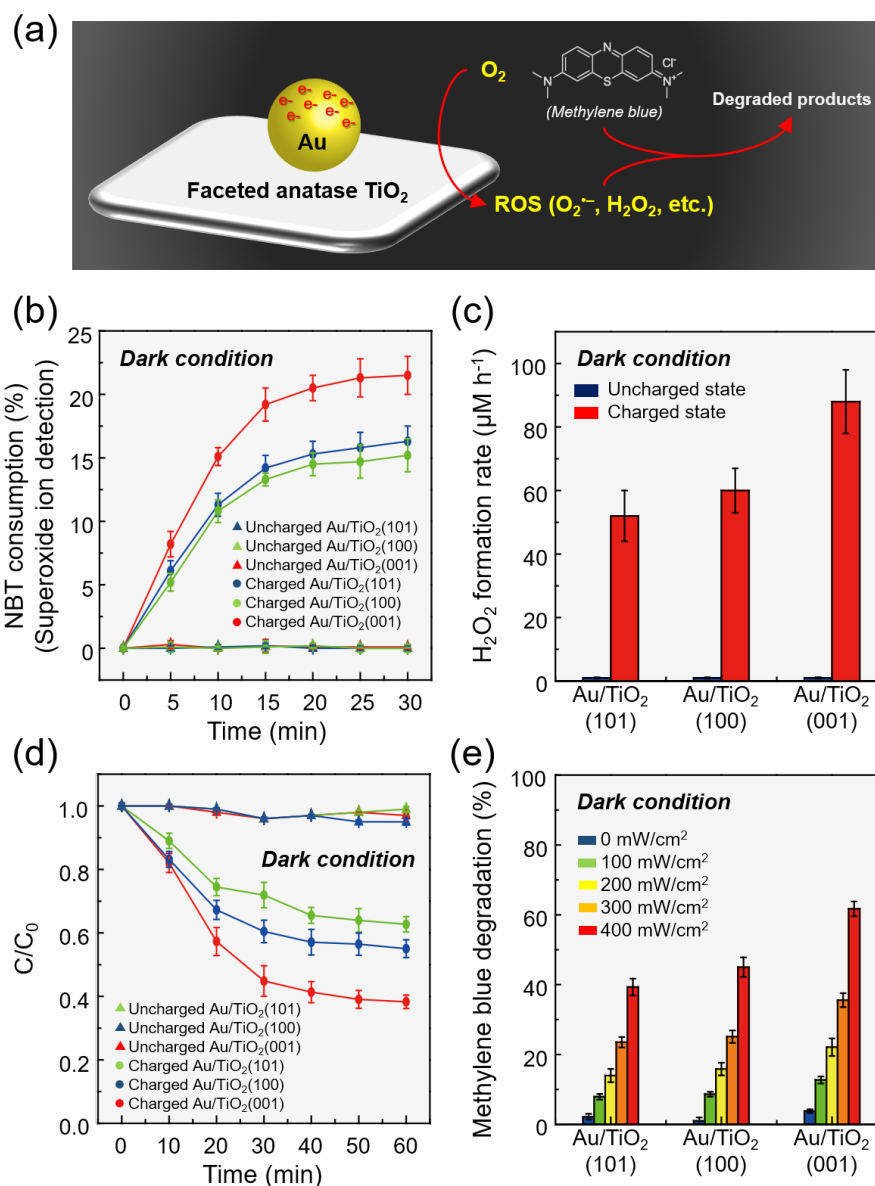


Figure 6. Facet-dependence of catalytic reactions in the dark following 1 hour of illumination. (a) Schematic of discharging process of photocharged Au/TiO₂. (b, c) Experimentally determined formation of (b) superoxide ion (O₂⁻) and (c) hydrogen peroxide (H₂O₂). (d) Methylene blue degradation in the dark by the different types of charged and uncharged Au/TiO₂, and (e) for different light intensities employed during photocharging process. In all cases, photocharging was conducted prior to the measurements in a fully N₂ purged solution for 1h. All dark-catalytic reactions were conducted in dark, aerobic conditions.

Facet-dependent catalytic reactions on Au/TiO₂ in the dark

To further substantiate the facet-dependence of light-induced electron charge storage of Au/TiO₂, we experimentally examined the ability of these systems to perform catalysis in dark, aerobic conditions following 1 h of irradiation in an anaerobic environment. First, we revisited the discharging of Au/TiO₂ when exposed to air. As illustrated in **Figure 6a**, the likely mechanism for discharging is that electrons trapped in vacant states of the Au during anaerobic light irradiation react with oxygen in the dark, generating reactive oxygen species (ROS). Specifically, the reduction of O₂ results in superoxide ions (O₂⁻), which then react with protons to produce hydrogen peroxide

(H₂O₂).³²⁻³⁴ To confirm this, we performed nitroblue tetrazolium (NBT) and 2,2'-azino-bis(3-ethylbenzothiazoline-6-sulphonic acid) (ABTS) assays to assess the presence of O₂⁻ and H₂O₂, respectively (**Figures S16-S18**). In the case of uncharged Au/TiO₂, no reduction of NBT was observed in the dark. In contrast, photocharged Au/TiO₂ NPs exhibited a progressive reduction of NBT, with Au/TiO₂(001) showing the largest decrease in NBT concentration over the measurement time of 30 min, 1.3 times larger than that achieved by the (101) and (100) systems (**Figure 6b**). Similar to O₂⁻ formation, uncharged Au/TiO₂ displayed negligible H₂O₂ generation in the dark, while the photocharged Au/TiO₂(101), (100), and (001) generated 52, 60, and 88 μM H₂O₂, respectively, under the dark and aerobic condition over the course of 1h (**Figure 6c**).

We further tested whether the ROS (O_2^- , H_2O_2) generated by the photocharged species could be implemented productively for the degradation of organic compounds in the dark. Methylene blue (MB) dye was employed as a molecular model. As shown in **Figure 6d** and **Figure S19**, uncharged Au/TiO₂ exhibited only a slight decrease in MB concentration (5%) over the course of 1 h, which is attributed to the adsorption effect rather than electron transfer.³⁵ Likewise, photocharged bare TiO₂ (without Au) exhibited a decrease of less than 10% in MB concentration for all three types of nanocrystals (**Figure S20**). In contrast, the MB concentration decreased by 38%, 45% and 61% for the Au/TiO₂(101), Au/TiO₂(100), and Au/TiO₂(001), respectively, highlighting the superior dark-catalytic performance of the {001} family of facets among the three types. We note that the effect is proportional to the light intensity during photocharging (**Figure 6e**).

Discussion

In these studies, we implemented electrochemical and photocatalytic experiments to determine the relative charge-storage ability of three different Au/TiO₂ systems distinguished by the majority facet of the TiO₂ nanocrystal. We found that Au/TiO₂(001) has the highest charge-storage capacity, current density, and photocatalytic activity in the dark following illumination, compared to Au/TiO₂(100) and Au/TiO₂(101). DFT calculations revealed that the prevalence of interfacial oxygen adatoms is the key to the electron transfer from excited TiO₂ to Au. The mechanism of charge transfer is illustrated in **Figure S21**, which shows that oxygen adatoms draw electrons away from Au, pulling the Fermi energy level of the Au further below the TiO₂ conduction band, thereby creating additional vacant states in Au for photogenerated electron storage.³⁶ Specifically, following light absorption, excitons are created in TiO₂ and the holes participate in oxidation reactions at the TiO₂ surface, while the electrons are transferred from the TiO₂ conduction band into the Au vacant states. This process can continue until the Fermi level of Au approaches the TiO₂ conduction band, when TiO₂ shows exciton bleaching,³⁶ thereby limiting the charge storage capacity of the system. The stored electrons can later participate in reactions in the presence of a reducing agent.

The highest electron-storage capacity observed for Au on the TiO₂{001} family of facets compared to {100} and {101} families is due to the highest coverage of oxygen adatoms at the Au/TiO₂(001) interface and is likely related to the differences in atomic arrangement and electronic structure of the different anatase facets. The TiO₂(001) facet exhibits a square lattice featuring five-fold coordinated Ti atoms and two-fold coordinated oxygen atoms.^{37,38} This configuration possesses a high density of under-coordinated Ti atoms, which can be stabilized by Au-O-Ti bond formation.^{39,40} Besides, the (001) facet possesses the lowest conduction band among anatase facets and hence is the most reactive for oxygen. In addition, the (001) facet generally exhibits the strongest adsorption capacity toward metals,⁴¹ which can lead to the formation of a Schottky junction and improved charge transfer between the TiO₂ and the deposited gold nanoparticles.

Through this work, we have thus uncovered a potential mechanism for electron charge transfer (and therefore storage) for gold nanoparticles deposited on TiO₂. However, some details will be of interest to consider in follow-up work. For example, water interacts differently on different TiO₂ surfaces, adsorbing

more strongly to the (001) facet than to the (100) and (101) facets.^{38,42} This motivates DFT studies for a water environment and/or experiments in air at various humidification. A limitation of the DFT is the computational constraints to the size of each component, with the rod being significantly smaller than the NPs. The ratio between interfacial and non-interfacial Au atoms is thus overestimated (38% in the model vs < 3 % for the ~9.5 nm particles used in the experiments). In further studies, we aim to investigate the influence of water adsorption and implement TiO₂ nanocrystals of more uniform size.

Conclusion

We used a combination of electrochemical characterizations, photochemical experiments, and DFT calculations to investigate the ability of gold nanoparticles deposited on anatase TiO₂ nanocrystals to store photogenerated charges, as a function of the dominant exposed family of facets of TiO₂: {101}, {100}, or {001}. As determined through cyclic voltammetry, the Au/TiO₂(001) system exhibited the highest peak current and longest decay time following illumination compared to the other two (and substantially higher than any of the three types of TiO₂ without AuNPs as well as for the AuNPs without TiO₂). The charge storage capacity was calculated from the CV measurements to be largest for Au/TiO₂(001), which also exhibited the highest production of reactive oxygen species and degradation of methylene blue after the illumination had been terminated. Our DFT results revealed that the Au/TiO₂(001) interface is more highly oxidized than the other two Au/TiO₂ types at temperature and O₂ partial pressure corresponding to the experimental conditions. The high number of interfacial oxygen adatoms results in depletion of electrons from Au, leading to more vacant states that can store excess electrons from TiO₂. We believe that crystal facet engineering is a key aspect to optimize crystalline materials for light energy storage and it is of great interest to further explore the role of the interface in such systems.

Experimental section

Materials. Titanium(IV) butoxide, potassium chloride (KCl), hydrofluoric acid (HF, 48%), nitroblue tetrazolium (NBT), peroxidase from horseradish (HRP), 2,2'-azino-bis(3-ethylbenzothiazoline-6-sulfonic acid) (ABTS), Tetrachloroauric(III) acid trihydrate (HAuCl₄ · 3H₂O), sodium citrate, tannic acid, sodium hydroxide (NaOH), hydrogen peroxide (H₂O₂, 35%), lithium chloride (LiCl) and potassium carbonate (K₂CO₃) were purchased from Sigma-Aldrich (St. Louis, MO USA). Titanium(IV) oxide particles (AEROXIDE® P25) were purchased from Thermo Fisher Scientific (Waltham, MA USA). Indium tin oxide (ITO) electrodes (7-10 ohm/sq, 20x40x1.1mm) were purchased from MSE Supplies LLC (Tucson, AZ USA).

Synthesis of TiO₂(101) and (100) nanocrystals. TiO₂(101) and (100) nanocrystals were prepared by referring to a previously reported two-step hydrothermal method.²² 16 g of NaOH were dissolved in 40 mL of deionized (DI) water in a 50 mL conical tube, and the solution was allowed to cool for 10 min at room temperature to dissipate the heat generated by the highly exothermic reaction. 1 g of P25 TiO₂ was added to the NaOH solution and thoroughly dispersed using an analog vortex mixer (Model 58816-121, VWR, USA). The mixture was transferred to a 50 mL Teflon-lined stainless-steel autoclave, followed by thermal treatment at 120 °C for 24 h. After cooling for 3 h at

room temperature, the contents were transferred to a conical tube and a white precipitate (sodium titanate) was collected by centrifugation at 11,000 rpm for 10 min and washed with DI water five times until the solution pH was between 10.2 and 10.7. The Na-titanate was dried at 50 °C for 24 h. (1) *TiO₂(101) nanocrystals*: 500 mg of Na-titanate and 30 ml of DI water were added into a 50 mL conical tube, and the Na-titanate solution was sonicated for 30 min and vigorously dispersed for 5 min using the vortex mixer (Model 58816-121, VWR, USA). After achieving full dispersion, 95 mg of LiCl was added to the Na-titanate solution, followed by vortexing for an additional 5 min. The mixture was transferred to a 100 mL Teflon-lined stainless-steel autoclave, which was placed in an oven at 200 °C for 20 h. This time was extended from the published value of 16 h to eliminate tiny nanoparticles and obtain well-defined bipyramidal structures. After incubation, the autoclave was cooled for 4 h at room temperature. The contents were transferred to a conical tube and the white precipitate was collected by centrifugation at 11,000 rpm for 15 min and washed with DI water at least five times. The final white product, identified as TiO₂(101), was obtained after drying at 60 °C for 24 h. (2) *TiO₂(100) nanocrystals*: 3 g of Na-titanate was divided equally into 4 conical tubes, each pre-filled with 38 mL of DI water. The Na-titanate solutions were sonicated for 30 min and vigorously dispersed for 5 min using the vortex mixer (Model 58816-121, VWR, USA). Once the dispersions were complete, 2 mL of H₂O₂, 35% was added to each conical tube, followed by gentle mixing for 5 min. The entire mixture (160 mL) was transferred to the 200 mL autoclave and stirred for an additional 15 min. The autoclave was then left in an oven at 180 °C for 20 h, after which it was allowed to cool for 4 h at room temperature. The white precipitate was gathered through centrifugation at 11,000 rpm for 15 min and rinsed with DI water for at least five times. The final white product, recognized as TiO₂(100), was obtained after drying at 60 °C for 24 h. The morphologies of TiO₂(101) and (100) were characterized by a transmission electron microscopy (TEM) (JEOL-2100F, JEOL, USA).

Synthesis of TiO₂(001) nanocrystals. TiO₂(001) nanocrystals were synthesized by referring to a published hydrothermal method.²⁴ 25 mL of titanium(IV) butoxide and 3 mL of hydrofluoric acid (HF, 48%) were added to a 100 mL Teflon-lined stainless-steel autoclave and stirred for 1 min using a polypropylene spatula with hollow core. Following incubation at 200 °C for 24 h, the reaction mixture was allowed to cool for 4 h at room temperature in a fume hood. The white precipitate was collected by centrifugation at 11,000 rpm for 15 min and washed alternately with DI water and ethanol at least five times. The white product was additionally washed with 1 M NaOH five more times to ensure the complete removal of adsorbed surface F-ions. The final white product, identified as TiO₂(001), was obtained after washing with DI water once more and drying at 60 °C for 24 h. The morphology of TiO₂(001) was characterized using a TEM (JEOL-2100F, JEOL, USA).

Synthesis of AuNPs. AuNPs of 9.5 nm in diameter were synthesized by citrate-mediated seeded-growth method.⁴⁴ A three-necked round-bottom flask was thoroughly cleaned using aqua regia. Subsequently, 600 mL of 2.2 mM sodium citrate, 0.4 mL of 2.5 mM tannic acid, 4 mL of 150 mM K₂CO₃ solution, and a magnetic stir bar were added to the flask, which was then placed in an oil bath on a hot plate magnetic stirrer, and stirred at 450 rpm at 70 °C for 30 min. The pH of the mixture was measured, and K₂CO₃ was added until the pH reached 10. Then, 4

mL of 25 mM HAuCl₄ solution was then injected into the mixture in the flask, and the mixture was allowed to react at 70 °C for 10 min. The color of the mixture rapidly changed to black-gray and then to orange-red within the following 2 min. After 10 min of reaction, the seeded-growth process of AuNPs was repeated as detailed below, for a total of four times (resulting in a total of 8 additional 2 mL of 25 mM HAuCl₄ injections) to obtain a final solution of 9.5 nm AuNPs. Seeded-growth process of AuNPs: In each repetition, 200 mL of the orange-red mixture was removed and replaced with an additional 200 mL of sodium citrate solution, followed by stirring for 30 min at 70 °C. Then, 2 mL of 25 mM HAuCl₄ solution was injected into the mixture and allowed to react for 10 min at 70 °C. Subsequently, another 2 mL of 25 mM HAuCl₄ solution was injected into the mixture and allowed to react for an additional 10 min at 70 °C. The dilution and injection steps were repeated until the AuNPs reached the desired size. In this report, we performed a total of four repetitions, resulting in a total of 8 additional 2 mL injections of a 25 mM HAuCl₄ solution.

Preparation of Au/TiO₂. The AuNPs were attached on the TiO₂ nanocrystals by using a published ligand-exchange method.⁴⁵ An ammonium hydroxide solution was prepared by adding 500 µL of NH₃·H₂O (28%) into 20 mL of DI water in a 50 mL conical tube. 50 mg of synthesized TiO₂ nanocrystals were then immersed in the solution for 24 h. The solution was then sonicated for 30 min to achieve complete dispersion of the nanocrystals, and then allowed to stand undisturbed overnight after which 250 µL of 3-mercaptopropionic acid (MPA) was added, followed by the addition of a calculated volume (9.36 mL) of the AuNP solution (here 0.75 mg to achieve 1.5 wt%). Upon adding the AuNPs, the color of the mixture changed from white to light-pink. The mixture was sonicated for 15 min, then vigorously stirred at 700 rpm on a magnetic stir plate for 30 min, and subsequently kept static overnight. This resulted in the TiO₂ bound to AuNPs settling at the bottom of the conical tube. The precipitate exhibited a light purple color. It was collected by centrifugation at 11,000 rpm for 15 min, washed with DI water four times, and dried at 60 °C for 24 h in a vacuum oven. The final product was obtained by annealing the dried light purple precipitate at 200 °C for 2 h. The morphologies of the thus prepared Au/TiO₂ (101), (100), and (001) were characterized using a TEM (JEOL-2100F, JEOL, USA).

Electrochemical characterization. The ITO electrodes were rinsed with DI water and ethanol and then treated with oxygen plasma at 50 W for 5 min (Diener electronic GmbH & Co. KG., Germany), to enhance the even spreading and adhesion of the active material (TiO₂, Au, or Au/TiO₂) solution on the glass surface. Afterwards, 400 µL of either the TiO₂, Au/TiO₂ (4 mg/mL), or AuNP solutions (0.06 mg/mL) were deposited onto the ITO glass electrode and fully dried at 60 °C for 2 h.

All electrochemical experiments were performed using a VersaSTAT 3 potentiostat (AMETEK Inc., USA) in a three-electrode system, consisting of Ag/AgCl (in 3 M NaCl) as the reference electrode and a graphite rod as the counter electrode. CV and CA measurements were conducted in a 1 M KCl electrolyte solution. For all analyses performed in anaerobic conditions, the electrolyte solution was first thoroughly purged with N₂ gas to remove oxygen. The scan rate was set at 100 mV/s. For the photocurrent measurements, a potential of 0.7 V (vs Ag/AgCl) was applied to the TiO₂ and Au/TiO₂-coated electrodes. To evaluate the photocharging storage capabilities of

TiO₂ and Au/TiO₂ NPs, CV analyses were conducted as follows: the TiO₂ and Au/TiO₂ electrodes were photocharged by an Xe lamp (Model No: 66924-450XF-R1, Newport Co., USA) irradiation (wavelength: 200-2500 nm, photon flux: 300 mW/cm²) under anaerobic conditions. Voltage profiles of the photocharged TiO₂ and Au/TiO₂ electrodes were measured immediately upon turning off the Xe lamp. Subsequently, these photocharged TiO₂ and Au/TiO₂-coated electrodes were transferred to a separate 1 M KCl solution and discharged in the absence of light while air was flowed through the solution. Following this, CV analysis was conducted in the initial electrolyte solution to evaluate the discharged state of both the TiO₂ and Au/TiO₂ electrodes.

Computational Studies. Density functional theory calculations are performed using the Vienna ab initio simulation package.⁴⁵⁻⁴⁷ The exchange-correlation energy is calculated using the Perdew-Burke-Ernzerhof functional.⁴⁸ The projector-augmented wave method is used to describe the core electrons.⁴⁹ The one-electron wave functions are developed on a basis set of plane waves with a 400 eV energy cutoff. To correct for the self-interaction error of Ti 3d electrons, a Hubbard-like repulsion term is added using Dudarev's approach, with $U_{\text{Ti}} = 3.5$ eV, determined using linear response.^{50,51} The Brillouin zone is sampled at the Gamma point only, since unit cell is large. Energy differences between steps in SCF cycles are converged to 10⁻⁶ eV. Atomic positions are relaxed until the forces are less than 0.05 eV/Å. The dDsc dispersion correction method is used to account for van der Waals forces.^{52,53} Surface charging with implicit solvation model is used to simulate the aqueous electrolyte, with 3.05 Å Debye length simulating 1 M KCl electrolyte.^{54,55} Bader charge analysis is employed to determine local charge of atoms.^{56,57}

Nitroblue tetrazolium (NBT) assay. The NBT assay is a spectrophotometric technique employed to detect the generation of superoxide ions (O₂⁻), which are reactive oxygen species. The reaction is shown in **Figure S16**. In this experiment, a 100 μM NBT solution was reacted with both photocharged and uncharged Au/TiO₂ NPs (2 mg/mL) under dark conditions to maintain an aerobic environment while purging with air gas. When exposed to superoxide ions (O₂⁻), NBT molecules (having an absorbance peak at 259 nm) are reduced to formazan, which exhibits an absorbance peak at 560 nm. The relative amount of generated superoxide ions can be determined by monitoring the decrease in absorbance at 259 nm, using a spectrophotometer (Product No. A23615, Beckman Coulter Inc., USA).

2,2'-azino-bis(3-ethylbenzothiazoline-6-sulphonic acid) (ABTS) assay. The ABTS assay is a spectrophotometric method used to detect the generation of hydrogen peroxide (H₂O₂); the reaction is depicted in **Figure S17**. The amount of H₂O₂ generated from Au/TiO₂ NPs was quantified using the ABTS assay, which relies on the oxidation of ABTS, catalyzed by horseradish peroxidase (HRP). In this procedure, 0.05 mL of reaction samples were combined with 0.95 mL of a mixture containing 2 mM ABTS and 2.5 U HRP. After a 10 min incubation period at room temperature, the absorbance of the mixture was monitored at 420 nm using a spectrophotometer (Product No. A23615, Beckman Coulter Inc., USA). The amount of H₂O₂ produced was calculated based on a pre-established calibration curve.

Dark catalytic degradation of methylene blue (MB). Before the dark-catalytic reactions, a conical tube filled with 5mL

of DI water in a conical tube was thoroughly purged with N₂ gas. TiO₂ or Au/TiO₂ NPs (10 mg) were then dispersed in the water and again N₂ gas purged. The particles were photocharged by illumination with the Xe lamp under anaerobic conditions with N₂ gas purging for 1 h. After switching light off, methylene blue (MB) dye (2 mg/mL) was added to the aqueous solution containing the photocharged Au/TiO₂ NPs, reaching a final concentration of 300 μM. The mixture was then allowed to react in the dark under aerobic conditions created by air purging for 1 hour. After the dark-catalytic reaction, Au/TiO₂ NPs were removed from MB solution by centrifugation. The MB solution was then diluted 10-fold in DI water, and the absorbance of the diluted MB solution was monitored at 662 nm using a spectrophotometer (Product No. A23615, Beckman Coulter Inc., USA). For the uncharged states, Au/TiO₂ NPs, which were maintained in the dark under anaerobic conditions with N₂ purging for 1 hour, were allowed to react with MB in the dark under aerobic conditions with air gas purging.

ASSOCIATED CONTENT

Supporting Information.

The Supporting Information is available free of charge on the ACS Publications website at DOI:

AUTHOR INFORMATION

Corresponding Author

* sautet@ucla.edu

* jaiz@seas.harvard.edu

Author Contributions

G.S. and J.A. conceived the conceptual idea. G.S. conducted all the experiments, analyzed the results, and prepared the manuscript. Y.L. and P.S. conducted all theoretical calculations based on density functional theory. A.V.S., M.A., and J.H.H. contributed to the experimental analysis and revised the manuscript. J.H.H. advised on the synthesis of Au/TiO₂. P.S. and J.A. supervised and guided the entire project. All authors have given approval to the final version of the manuscript.

Notes

The authors declare no competing financial interest.

ACKNOWLEDGMENT

This study was supported by the U.S. Defense Threat Reduction Agency (DTRA) under Award Number HDTR1211001612. The authors thank Kang Rui Garrick Lim, and Sadhya Garg for fruitful scientific discussion.

REFERENCES

- (1) Tong, H.; Ouyang, S.; Bi, Y.; Umezawa, N.; Oshikiri, M.; Ye, J. Nano-photocatalytic Materials: Possibilities and Challenges. *Adv. Mater.* **2012**, *24*, 229-251.
- (2) Sivula, K.; van de Krol, R. Semiconducting materials for photoelectrochemical energy conversion. *Nat. Rev. Mater.* **2016**, *1*, 15010.
- (3) Ngaotrakanwivat, P.; Tatsuma, T.; Saitoh, S.; Ohko, Y.; Fujishima, A. Charge-discharge behavior of TiO₂-WO₃ photocatalysis systems with energy storage ability. *Phys. Chem. Chem. Phys.* **2003**, *5*, 3234-3237.
- (4) Tatsuma, T.; Saitoh, S.; Ngaotrakanwivat, P.; Ohko, Y.; Fujishima, A. Energy Storage of TiO₂-WO₃ Photocatalysis Systems in the Gas Phase. *Langmuir* **2002**, *18*, 7777-7779.
- (5) Tatsuma, T.; Saitoh, S.; Ohko, Y.; Fujishima, A. TiO₂-WO₃ Photoelectrochemical Anticorrosion System with an Energy Storage Ability. *Chem. Mater.* **2001**, *13*, 2838-2842.

- (6) Cai, T.; Liu, Y.; Wang, L.; Dong, W.; Zeng, G. Recent advances in round-the-clock photocatalytic system: Mechanisms, characterization techniques and applications. *J. Photochem. Photobiol. C: Photochem. Rev.* **2019**, *39*, 58-75.
- (7) Loh, J. Y. Y.; Sharma, G.; Kherani, N. P.; Ozin, G. A. Post-Illumination Photoconductivity Enables Extension of Photo-Catalysis after Sunset. *Adv. Energy Mater.* **2021**, *11*, 2101566.
- (8) Cai, T.; Liu, Y.; Wang, L.; Zhang, S.; Ma, J.; Dong, W.; Zeng, Y.; Yuan, J.; Liu, C.; Luo, S. "Dark Deposition" of Ag Nanoparticles on TiO₂: Improvement of Electron Storage Capacity To Boost "Memory Catalysis" Activity. *ACS Appl. Mater. Interfaces* **2018**, *10*, 25350-25359.
- (9) Takai, A.; Kamat, P. V. Capture, Store, and Discharge. Shuttling Photogenerated Electrons across TiO₂-Silver Interface. *ACS Nano* **2011**, *5*, 7369-7376.
- (10) Chiu, Y.-H.; Hsu, Y.-J. Au@Cu₇S₄ yolk@shell nanocrystal-decorated TiO₂ nanowires as an all-day-active photocatalyst for environmental purification. *Nano Energy* **2017**, *31*, 286-295.
- (11) Liu, D.; Zi, W.; Sajjad, S. D.; Hsu, C.; Shen, Y.; Wei, M.; Liu, F. Reversible Electron Storage in an All-Vanadium Photoelectrochemical Storage Cell: Synergy between Vanadium Redox and Hybrid Photocatalyst. *ACS Catal.* **2015**, *5*, 2632-2639.
- (12) Lightcap, I. V.; Kosel, T. H.; Kamat, P. V. Anchoring Semiconductor and Metal Nanoparticles on a Two-Dimensional Catalyst Mat. Storing and Shuttling Electrons with Reduced Graphene Oxide. *Nano Lett.* **2010**, *10*, 577-583.
- (13) Park, J. Y.; Baker, L. R.; Somorjai, G. A. Role of Hot Electrons and Metal-Oxide Interfaces in Surface Chemistry and Catalytic Reactions. *Chem. Rev.* **2015**, *115*, 2781-2817.
- (14) Miller, D. R.; Akbar, S. A.; Morris, P. A. Nanoscale metal oxide-based heterojunctions for gas sensing: A review. *Sens. Actuators, B* **2014**, *204*, 250-272.
- (15) Gao, M.; Wang, L.; Yang, Y.; Sun, Y.; Zhao, X.; Wan, Y. Metal and Metal Oxide Supported on Ordered Mesoporous Carbon as Heterogeneous Catalysts. *ACS Catal.* **2023**, *13*, 4060-4090.
- (16) Cao, S.; Tao, F.; Tang, Y.; Li, Y.; Yu, J. Size- and shape-dependent catalytic performances of oxidation and reduction reactions on nanocatalysts. *Chem. Soc. Rev.* **2016**, *45*, 4747-4765.
- (17) Fu, C.; Li, F.; Zhang, J.; Li, D.; Qian, K.; Liu, Y.; Tang, J.; Fan, F.; Zhang, Q.; Gong, X.-Q.; Huang, W. Site Sensitivity of Interfacial Charge Transfer and Photocatalytic Efficiency in Photocatalysis: Methanol Oxidation on Anatase TiO₂ Nanocrystals. *Angew. Chem., Int. Ed.* **2021**, *60*, 6160-6169.
- (18) Yu, J.; Low, J.; Xiao, W.; Zhou, P.; Jaroniec, M. Enhanced Photocatalytic CO₂-Reduction Activity of Anatase TiO₂ by Coexposed {001} and {101} Facets. *J. Am. Chem. Soc.* **2014**, *136*, 8839-8842.
- (19) Wei, T.; Ding, P.; Wang, T.; Liu, L.-M.; An, X.; Yu, X. Facet-Regulating Local Coordination of Dual-Atom Cocatalyzed TiO₂ for Photocatalytic Water Splitting. *ACS Catal.* **2021**, *11*, 14669-14676.
- (20) Gao, Y.; Nie, W.; Zhu, Q.; Wang, X.; Wang, S.; Fan, F.; Li, C. The Polarization Effect in Surface-Plasmon-Induced Photocatalysis on Au/TiO₂ Nanoparticles. *Angew. Chem., Int. Ed.* **2020**, *59*, 18218-18223.
- (21) Bian, Z.; Tachikawa, T.; Zhang, P.; Fujitsuka, M.; Majima, T. Au/TiO₂ Superstructure-Based Plasmonic Photocatalysts Exhibiting Efficient Charge Separation and Unprecedented Activity. *J. Am. Chem. Soc.* **2014**, *136*, 458-465.
- (22) Tang, M.; Li, S.; Chen, S.; Ou, Y.; Hiroaki, M.; Yuan, W.; Zhu, B.; Yang, H.; Gao, Y.; Zhang, Z.; Wang, Y. Facet-Dependent Oxidative Strong Metal-Support Interactions of Palladium-TiO₂ Determined by In Situ Transmission Electron Microscopy. *Angew. Chem., Int. Ed.* **2021**, *60*, 22339-22344.
- (23) Li, D.; You, R.; Yang, M.; Liu, Y.; Qian, K.; Chen, S.; Cao, T.; Zhang, Z.; Tian, J.; Huang, W. Morphology-Dependent Evolutions of Sizes, Structures, and Catalytic Activity of Au Nanoparticles on Anatase TiO₂ Nanocrystals. *J. Phys. Chem. C* **2019**, *123*, 10367-10376.
- (24) Li, C.; Koenigsman, C.; Ding, W.; Rudshteyn, B.; Yang, K. R.; Regan, K. P.; Konezny, S. J.; Batista, V. S.; Brudvig, G. W.; Schmuttenmaer, C. A.; Kim, J.-H. Facet-Dependent Photoelectrochemical Performance of TiO₂ Nanostructures: An Experimental and Computational Study. *J. Am. Chem. Soc.* **2015**, *137*, 1520-1529.
- (25) Chen, J.-J.; Wu, J. C. S.; Wu, P. C.; Tsai, D. P. Improved Photocatalytic Activity of Shell-Isolated Plasmonic Photocatalyst Au@SiO₂/TiO₂ by Promoted LSPR. *J. Phys. Chem. C* **2012**, *116*, 26535-26542.
- (26) Sellappan, R.; Nielsen, M. G.; González-Posada, F.; Vesborg, P. C. K.; Chorkendorff, I.; Chakarov, D. Effects of plasmon excitation on photocatalytic activity of Ag/TiO₂ and Au/TiO₂ nanocomposites. *J. Catal.* **2013**, *307*, 214-221.
- (27) Yuan, W.; Zhu, B.; Fang, K.; Li, X.-Y.; Hansen, T. W.; Ou, Y.; Yang, H.; Wagner, J. B.; Gao, Y.; Wang, Y.; Zhang, Z. In situ manipulation of the active Au-TiO₂ interface with atomic precision during CO oxidation. *Science* **2021**, *371*, 517-521.
- (28) Duan, Z.; Henkelman, G. CO Oxidation at the Au/TiO₂ Boundary: The Role of the Au/Ti_{5c} Site. *ACS Catal.* **2015**, *5*, 1589-1595.
- (29) Lazzeri, M.; Vittadini, A.; Selloni, A. Structure and energetics of stoichiometric TiO₂ anatase surfaces. *Phys. Rev. B* **2001**, *63*, 155409.
- (30) Laursen, S.; Linic, S. Geometric and electronic characteristics of active sites on TiO₂-supported Au nano-catalysts: insights from first principles. *Phys. Chem. Chem. Phys.* **2009**, *11*, 11006-11012.
- (31) Laursen, S.; Linic, S. Strong Chemical Interactions Between Au and Off-Stoichiometric Defects on TiO₂ as a Possible Source of Chemical Activity of Nanosized Au Supported on the Oxide. *J. Phys. Chem. C* **2009**, *113*, 6689-6693.
- (32) Saito, I.; Matsuura, T.; Inoue, K. Formation of superoxide ion via one-electron transfer from electron donors to singlet oxygen. *J. Am. Chem. Soc.* **1983**, *105*, 3200-3206.
- (33) Goto, H.; Hanada, Y.; Ohno, T.; Matsumura, M. Quantitative analysis of superoxide ion and hydrogen peroxide produced from molecular oxygen on photoirradiated TiO₂ particles. *J. Catal.* **2004**, *225*, 223-229.
- (34) Jalilov, A. S.; Zhang, C.; Samuel, E. L. G.; Sikkema, W. K. A.; Wu, G.; Berka, V.; Kent, T. A.; Tsai, A.-L.; Tour, J. M. Mechanistic Study of the Conversion of Superoxide to Oxygen and Hydrogen Peroxide in Carbon Nanoparticles. *ACS Appl. Mater. Interfaces* **2016**, *8*, 15086-15092.
- (35) Han, J. H.; Shneidman, A. V.; Kim, D. Y.; Nicolas, N. J.; van der Hoeven, J. E. S.; Aizenberg, M.; Aizenberg, J. Highly Ordered Inverse Opal Structures Synthesized from Shape-Controlled Nanocrystal Building Blocks. *Angew. Chem., Int. Ed.* **2022**, *61*, e202111048.
- (36) Wood, A.; Giersig, M.; Mulvaney, P. Fermi Level Equilibration in Quantum Dot-Metal Nanojunctions. *J. Phys. Chem. B* **2001**, *105*, 8810-8815.
- (37) Nguyen, C. K.; Cha, H. G.; Kang, Y. S. Axis-Oriented, Anatase TiO₂ Single Crystals with Dominant {001} and {100} Facets. *Cryst. Growth Des.* **2011**, *11*, 3947-3953.
- (38) Vittadini, A.; Selloni, A.; Rotzinger, F. P.; Grätzel, M. Structure and Energetics of Water Adsorbed at TiO₂ Anatase (101) and (001) Surfaces. *Phys. Rev. Lett.* **1998**, *81*, 2954-2957.
- (39) Henkel, B.; Neubert, T.; Zabel, S.; Lamprecht, C.; Selhuber-Unkel, C.; Rätzke, K.; Strunskus, T.; Vergöhl, M.; Faupel, F. Photocatalytic properties of titania thin films prepared by sputtering versus evaporation and aging of induced oxygen vacancy defects. *Appl. Catal., B* **2016**, *180*, 362-371.
- (40) Zhang, J.; Chen, W.; Xi, J.; Ji, Z. {001} Facets of anatase TiO₂ show high photocatalytic selectivity. *Mater. Lett.* **2012**, *79*, 259-262.
- (41) Liao, J.; Yang, F.; Wang, C.-Z.; Lin, S. The crystal facet-dependent electrochemical performance of TiO₂ nanocrystals for heavy metal detection: Theoretical prediction and experimental proof. *Sens. Actuators, B* **2018**, *271*, 195-202.
- (42) Selloni, A. Anatase shows its reactive side. *Nat. Mater.* **2008**, *7*, 613-615.
- (43) Piella, J.; Bastús, N. G.; Puentes, V. Size-Controlled Synthesis of Sub-10-nanometer Citrate-Stabilized Gold Nanoparticles and Related Optical Properties. *Chem. Mater.* **2016**, *28*, 1066-1075.
- (44) Ding, D.; Liu, K.; He, S.; Gao, C.; Yin, Y. Ligand-Exchange Assisted Formation of Au/TiO₂ Schottky Contact for Visible-Light Photocatalysis. *Nano Lett.* **2014**, *14*, 6731-6736.
- (45) Kresse, G.; Furthmüller, J. Efficient iterative schemes for ab initio total-energy calculations using a plane-wave basis set. *Phys. Rev. B* **1996**, *54*, 11169-11186.

- (46) Kresse, G.; Furthmüller, J. Efficiency of ab-initio total energy calculations for metals and semiconductors using a plane-wave basis set. *Comput. Mater. Sci.* **1996**, *6*, 15-50.
- (47) Kresse, G.; Hafner, J. Ab initio molecular dynamics for liquid metals. *Phys. Rev. B* **1993**, *47*, 558-561.
- (48) Perdew, J. P.; Burke, K.; Ernzerhof, M. Generalized Gradient Approximation Made Simple. *Phys. Rev. Lett.* **1996**, *77*, 3865-3868.
- (49) Kresse, G.; Joubert, D. From ultrasoft pseudopotentials to the projector augmented-wave method. *Phys. Rev. B* **1999**, *59*, 1758-1775.
- (50) Aschauer, U.; Chen, J.; Selloni, A. Peroxide and superoxide states of adsorbed O₂ on anatase TiO₂ (101) with subsurface defects. *Phys. Chem. Chem. Phys.* **2010**, *12*, 12956-12960.
- (51) Dudarev, S. L.; Botton, G. A.; Savrasov, S. Y.; Humphreys, C. J.; Sutton, A. P. Electron-energy-loss spectra and the structural stability of nickel oxide: An LSDA+U study. *Phys. Rev. B* **1998**, *57*, 1505-1509.
- (52) Steinmann, S. N.; Corminboeuf, C. Comprehensive Benchmarking of a Density-Dependent Dispersion Correction. *J. Chem. Theory Comput.* **2011**, *7*, 3567-3577.
- (53) Steinmann, S. N.; Corminboeuf, C. A generalized-gradient approximation exchange hole model for dispersion coefficients. *J. Chem. Phys.* **2011**, *134*, 044117.
- (54) Mathew, K.; Kolluru, V. S. C.; Mula, S.; Steinmann, S. N.; Hennig, R. G. Implicit self-consistent electrolyte model in plane-wave density-functional theory. *J. Chem. Phys.* **2019**, *151*, 234101.
- (55) Mathew, K.; Sundararaman, R.; Letchworth-Weaver, K.; Arias, T. A.; Hennig, R. G. Implicit solvation model for density-functional study of nanocrystal surfaces and reaction pathways. *J. Chem. Phys.* **2014**, *140*, 084106.
- (56) Tang, W.; Sanville, E.; Henkelman, G. A grid-based Bader analysis algorithm without lattice bias. *J. Phys.: Condens. Matter* **2009**, *21*, 084204.
- (57) Henkelman, G.; Arnaldsson, A.; Jónsson, H. A fast and robust algorithm for Bader decomposition of charge density. *Comput. Mater. Sci.* **2006**, *36*, 354-360.

